Triplet emission of atomic ytterbium isolated in a xenon matrix

N. N. Kleshchina, I. S. Kalinina, R. Lambo, A. A. Buchachenko (iD), D. S. Bezrukov (iD), and S.-M. Hu

View Online   Export Citation   CrossMark

ARTICLES YOU MAY BE INTERESTED IN

Triplet emission of atomic ytterbium isolated in a xenon matrix

N. N. Kleshchina,[1] I. S. Kalinina,[2] R. Lambo,[3,a] A. A. Buchachenko,[2,b] (ID) D. S. Bezrukov,[1,2] (ID) and S.-M. Hu[4]

AFFILIATIONS

[1]Department of Chemistry, M.V. Lomonosov Moscow State University, Moscow 119991, Russia
[2]Skolkovo Institute of Science and Technology, Skolkovo Innovation Center, Moscow 121205, Russia
[3]Shenzhen Institutes of Advanced Technology, Chinese Academy of Sciences, Shenzhen 518055, China
[4]Hefei National Laboratory for Physical Sciences at the Microscale, Collaborative Innovation Center of Chemistry for Energy Materials, University of Science and Technology of China, Hefei 230026, China

[a]E-mail: lambo@mail.ustc.edu.cn
[b]E-mail: a.buchachenko@skoltech.ru

ABSTRACT

The electronic transitions of ytterbium atoms in a solid Xe matrix grown at 4.8 K are investigated. Absorption bands are detected in the regions of the gas-phase $6s^2\ {}^1S_0 \to 4f^{13}5d6s^2$ and $6s^2\ {}^1S_0 \to 6s6p\ {}^1P_1$ transitions. Both bands indicate that Yb atoms occupy multiple trapping sites, of which three are identified. Emission induced by the $6s^2\ {}^1S_0 \to 6s6p\ {}^1P_1$ excitation is found to be concentrated entirely in the region of the $6s6p\ {}^3P_J \to 6s^2\ {}^1S_0$ decay, whereas the singlet emission is completely quenched. Multiple emission peaks are observed and the effects of annealing and prolonged irradiation on their amplitudes are found to be significant and are interpreted as a consequence of Yb population transfer from one type of site to another. Modeling of the ground-state site structure and stability predicts three Yb/Xe occupation types, substitutional (ss), tetravacancy (tv) and hexavacancy (hv), in order of decreasing stability. Their tentative associations with observed absorption and emission features are discussed. Time correlated single photon spectroscopy is used to determine the lifetimes of the individual emission bands. They are found to be different from each other with indications of a mixture of short- and long- lived $6s6p\ {}^3P_J$ fine-structure components and demonstrate distinct temperature dependencies. A dramatic decrease in the lifetime of the emission peak tentatively assigned to the most stable site with temperature is explained by a competition between the radiative and non-radiative decay paths of the $6s6p\ {}^3P_1$ state. The mechanism of the latter can be attributed to electron–phonon coupling as confirmed by a model of the temperature-dependence of the lifetime.

1. INTRODUCTION

The photophysical properties of the ytterbium atom are currently an active research topic as a result of the creation of degenerate quantum gases of a variety of Yb isotopes[1–3] and their potential applications, which include a prospective atomic frequency standard.[4] Rare gas (RG) solids acting as matrix hosts offer a number of advantages for studying these properties, such as long storage and observation times, and have notably been used in the first measurement of the decay rate of the ^{171}Yb $6s6p\ {}^3P_0 \to 6s^2\ {}^1S_0$ clock transition.[5] Another precision experiment aims to use the strong Yb $6s6p\ {}^3P_1 \to 6s^2\ {}^1S_0$ decay in a proof-of-principle demonstration of the spectroscopy of a single atom isolated in a solid RG—a technique which can then be extended for use in detecting rare nuclear reactions.[6]

Both these experiments rely on the strong propensity of Yb isolated in the rare gases (RGs) for non-radiative relaxation following $6s^2\ {}^1S_0 \to 6s6p\ {}^1P_1$ excitation. In particular, it was shown that matrix isolation facilitates the singlet-to-triplet state population transfer by several orders of magnitude.[7] Previous works by our group[8,9] identified the mechanism behind this phenomenon as highly efficient intersystem crossing between the $6s6p\ {}^1P_1$ state and the nearby $6s5d\ {}^3D_J$ manifold[10] (see Fig. 1). The efficiency of this population transfer increases with the heaviness of the rare gas. In solid Ne, some singlet emission from the excited $6s6p\ {}^1P_1$ state is observed accompanied by the emissions from the $6s5d\ {}^3D_{1,2}$ and $6s6p\ {}^3P_{0,1}$ states.[8] In solid Ar, however, singlet emission is completely quenched and decay is concentrated in the $6s6p\ {}^3P_1 \to 6s^2\ {}^1S_0$ channel.[9]
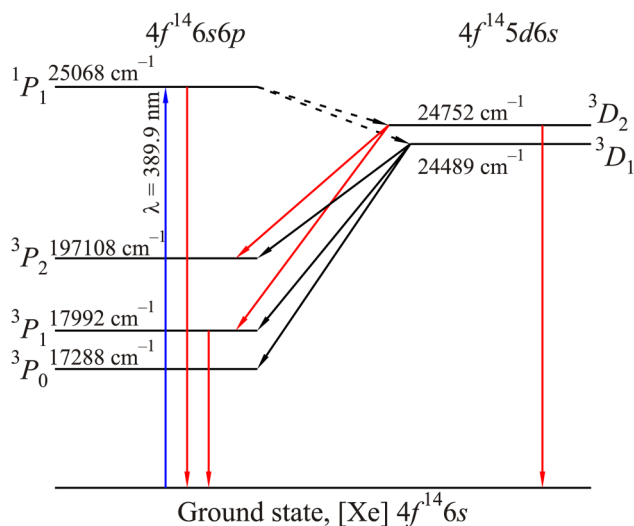
FIG. 1. Diagram of the relevant low-lying electronic energy levels of the Yb atom in the gas phase.[10] Allowed electric dipole transitions are shown by solid lines while those not allowed are shown by dashed lines.

In this paper, we present the first results of the emission spectroscopy of Yb isolated in a solid Xe matrix grown at 4.8 K. As with the Yb/Ar system, singlet emission induced by the $6s^2$ $^1S_0 \rightarrow 6s6p$ $^1P_1$ excitation was found to be completely quenched in Xe. Instead, four emission peaks appear in the region of the $6s6p$ $^3P_J \rightarrow 6s^2$ $^1S_0$ transition. It was also observed that heating and irradiation could alter the relative amplitudes of the emission peaks, which was interpreted in terms of the changes in Yb populations of the distinct trapping sites similar to those we observed in the Ar matrix.[9] In keeping with these findings, an investigation of the effect of temperature on the triplet state life-times revealed distinct decay dynamics for each site. The most notable effect is on the decay rate of the emission band tentatively associated with the most stable trapping site which increases dramatically with temperature due to competition between radiative decay and a highly efficient non-radiative process identified as electron–phonon coupling.

Absorption bands were detected in the regions of the gas-phase $6s^2$ $^1S_0 \rightarrow 4f^{13}5d6s^2$ and $6s^2$ $^1S_0 \rightarrow 6s6p$ $^1P_1$ transitions. These congested broad bands also revealed the presence of multiple trapping sites, among which three are reliably discernible. Their corresponding spectral features are labeled "red", "blue" and "violet" according to their relative frequencies. In support of these results, classical modeling of Yb in Xe was performed. It predicts three types of stable trapping sites, a single-substitutional (*ss*) vacancy, a tetravacancy (*tv*) and a hexavacancy (*hv*). Tentative assignment of these occupations with the observed spectral features associates the violet feature with *hv* occupation, the blue feature with *tv* occupation and the red feature with *ss* occupation.

The remainder of this paper is organized as follows. Section 2 details the experimental methods, while Sec. 3 describes the main results. In Sec. 4 we discuss our interpretations of the stable trapping sites, their transformations and relaxation pathways including that assisted by electron–phonon coupling. Concluding remarks follow.

2. EXPERIMENTAL SETUP

The Xe crystal was grown on a 1 in. diameter BaF_2 window which acted as a substrate. This was mounted in a holder thermally anchored to the coldhead of a closed-cycle helium refrigerator (Janis SHI-4-5) in a sample chamber evacuated to a pressure of 10^{-5} Pa. To implant the Yb atoms, an atomic beam produced by a Knudsen effusion oven was directed at the substrate together with a small Xe flux. Typical operating parameters were a substrate temperature of 4.8 K, an oven temperature of 344 °C and a gas flux of 0.45 SCCM maintained by a mass flow controller (MKS 1479A). Since solid Xe has the lowest transparency of all the RG matrices, for absorption spectroscopy the samples were grown over 10–15 minutes. For emission spectroscopy, however, they were grown over approximately 1 hour.

The spectrometer used for UV-visible excitation was the Thorlabs CCS 2000 model capable of a resolution of 0.5 nm. Light from a Xe lamp passing directly through the matrix was used for continuous white-light absorption spectroscopy. The light source for emission spectroscopy was a 405 nm centered diode laser (CNI Laser MDL-III-405) with a linewidth of 0.1 nm. This laser could be shutdown in ∼100 ns using an AOM (ISOMET 1206C-2-1002) for life-time measurements by standard Time Correlated Single Photon Spectroscopy (TCSPS), performed together with a single photon counting module (Perkin Elmer AQR-12 SPCM) and a DAQ card (National Instruments 6321 X) capable of a 10 ns time resolution.

The temperature of the system was controlled by a cartridge heater mounted on the coldhead and controlled by a PID loop. The temperature of the BaF_2 window could thus be stabilized to within 0.2 K between 4.2 K and 60 K during annealing cycles. Its temperature was monitored using a silicon diode sensor (DT-470) mounted on the baseplate holding the substrate.

3. RESULTS

3.1. Absorption spectra

An overview of the UV-visible absorption spectra of the freshly deposited Yb/Xe sample is shown in Fig. 2(a). Three main features are visible. Two of them, appearing in the 355–365 nm and 390–420 nm ranges, are assigned, respectively, to the $6s^2$ $^1S_0$ $4f^{13}5d6s^2$ and $6s^2$ $^1S_0$ $6s6p$ $^1P_1$ transitions whose respective gas-phase frequencies are nearest to them. These assignments are in agreement with those made in earlier work in which Yb deposited in Xe by laser ablation produced absorption bands centered at 358 and 403 nm.[11] The origin of the third feature at 367–392 nm is unclear. Due to the low transparency of the Xe matrix, we measured the transmittance with reference to a clean BaF_2 window, which may result in distortions to the baseline and the appearance of artificial features. We believe that the absorption feature at 380 nm is spurious, though it is also possible to attribute it to the $6s^2$ $^1S_0 \rightarrow 4f^{13}5d6s^2$ transition in dimers and larger clusters. All three of these features withstand annealing to 35 K for 10 minutes. Figure 2(b) presents an enlarged view of the band in the ultraviolet range which has a clear doublet structure. Annealing slightly distorts its contour making it more extended to the blue. The band peaked at 405 nm also has a doublet structure superimposed over a shoulder extending up to 420 nm, as shown in Fig. 2(c). Annealing preserves
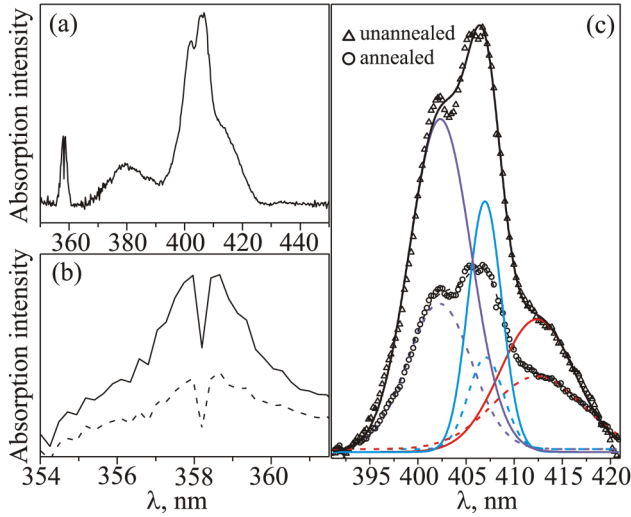
FIG. 2. Overview of the white-light normalized absorption spectra of the Yb/Xe system (a). Absorption spectra in the region of the $6s^2\ ^1S_0 \rightarrow 4f^{13}5d6s^2$ transition (b). Absorption spectra in the region of the $6s^2\ ^1S_0 \rightarrow 6s6p\ ^1P_1$ transition (c). The results of three-component Gaussian decompositions are also shown. The solid line represents the spectra of an unannealed sample, while the dashed line represents those of a sample annealed to 35 K for 10 minutes.

these structures, apparently making the shoulder more prominent. To investigate the effects of annealing more quantitatively, we decomposed the bands into three Gaussian components illustrated in Fig. 2(c). Independent fits of the bands recorded for the freshly deposited and annealed samples agree in the position of their components to within 0.2 nm, which adds certainty to such an analysis. The main features of the absorption spectra, which we will hereinafter refer to as "violet" and "blue" peaks and as a "red" shoulder, are summarized in the Table I.

Relying on spectral decomposition, we infer that the ratio of the violet:blue:red peak intensities changes upon annealing from 1:0.78:0.47 to 1:0.72:0.62, i.e., the red and, in part, the blue components gain in intensity at the expense of the violet one. It should be noted that the amplitudes of the absorption peaks in the annealed matrix are approximately half those of the unannealed sample. This is likely due to a decrease in the transparency of the matrix during heating rather than to a loss of Yb atoms. Based on the observed behavior, we attribute the three identified features to three distinct trapping sites, stable under annealing to 35 K. Though the present analysis is not exhaustive and does not rule out contributions from other sites, including unstable ones, it finds support in the emission spectroscopy and the site structure and stability simulations discussed below.

3.2. Emission spectra

In agreement with earlier results for the Yb/Ar system, the emission observed by exciting the $6s^2\ ^1S_0 \rightarrow 6s6p\ ^1P_1$ transition of the Yb/Xe sample is entirely concentrated in the frequency range characteristic of the $6s6p\ ^3P_J \rightarrow 6s^2\ ^1S_0$ transitions. For the free

TABLE I. Principal features of the absorption spectra of the Yb/Xe system. Here λ and ν refer respectively to the wavelength and transition frequency; δ refers to the matrix frequency shift relative to the gas phase transition frequency and Δ represents the FWHM. Results of the Gaussian decomposition are given in square brackets. An uncertainty of $\pm 40\ \mathrm{cm}^{-1}$ is assumed on all values.

Transition	λ, nm	ν, cm^{-1}	δ, cm^{-1}	Δ, cm^{-1}
Violet peaks				
$6s^2\ ^1S_0 \rightarrow 4f^{13}5d6s^2$	358.0	27935	−921	−
$6s^2\ ^1S_0 \rightarrow 6s6p\ ^1P_1$	402.3	[24856]	−211	−
	[402.2]	[24863]	[−205]	[600]
Blue peaks				
$6s^2\ ^1S_0 \rightarrow 4f^{13}5d6s^2$	358.6	27881	−976	−
$6s^2\ ^1S_0 \rightarrow 6s6p\ ^1P_1$	406.3	24615	−456	−
	[407.1]	[24564]	[−504]	[370]
Red shoulder				
$6s^2\ ^1S_0 \rightarrow 6s6p\ ^1P_1$	[412.4]	[24248]	[−820]	[1010]

atom, the allowed $6s6p\ ^3P_1 \rightarrow 6s^2\ ^1S_0$ transition occurs at 555.8 nm and the strongly forbidden $6s6p\ ^3P_0 \rightarrow 6s^2\ ^1S_0$ transition occurs at 578.1 nm.[10] Figure 3 shows that 405 nm laser excitation of the sample produces spectra dominated by two peaks at 564 and 605 nm, with two weaker features appearing at 655 nm and 711 nm (see Table II).

Lifetime measurements were performed using bandpass filters centered at 565 nm and 605 nm (FWHM 10 nm) in order to isolate each peak and the results are summarized in Table III. As shown in
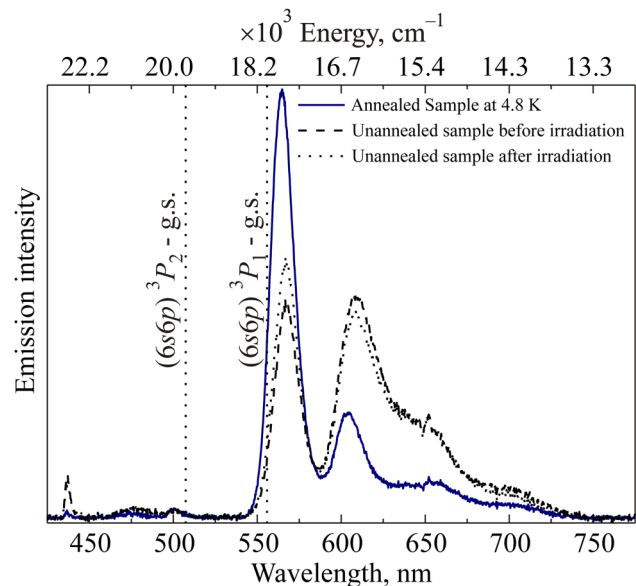

FIG. 3. Emission spectra of the Yb/Xe system excited with a laser centered at 405 nm. Irradiation was undertaken over a 3 minute period.

TABLE II. Principal features of the emission spectrum for the annealed Yb/Xe system resulting from $6s^2\ ^1S_0 \rightarrow 6s6p\ ^1P_1$ excitation at 4.8 K. The symbols here are the same as those used in Table I. The uncertainty is assumed to be $\pm 40\ cm^{-1}$ on all values.

Transition	λ, nm	ν, cm^{-1}	δ, cm^{-1}	Δ, cm^{-1}
$6s6p\ ^3P_1 \rightarrow 6s^2\ ^1S_0$	564.4	17733	499	−259
$6s6p\ ^3P_1 \rightarrow 6s^2\ ^1S_0$	605.3	16521	588	−1470
$6s6p\ ^3P_1 \rightarrow 6s^2\ ^1S^*_0$	654.9	15268	–	−2020
$6s6p\ ^3P_1 \rightarrow 6s^2\ ^1S^*_0$	710.7	14071	–	−2513

Fig. 4, the time-dependence of the normalized counts (NC) for the peak centered at 564 nm is exponential and gives a lifetime of $\tau = 382 \pm 2$ ns at 4.8 K, which is comparable to the gas-phase value of 866 ± 7 ns for the $6s6p\ ^3P_1 \rightarrow 6s^2\ ^1S_0$ transition.[12] Moreover, it fits the trend of a decrease in the triplet state lifetime as the heaviness of the rare-gas matrix increases. Measurements by the Argonne group give 680 ± 20 and 549 ± 8 ns for the $6s6p\ ^3P_1 \rightarrow 6s^2\ ^1S_0$ decay in Ne and Ar, respectively.[5]

Figure 5 shows that the decay of the 605 nm peak is complex and must be fitted to a double exponential of the form $NC = A_1 e_1^{-t/\tau} + A_2 e_2^{-t/\tau}$. At 4.8 K we obtain the values of $A_1 = 0.7256 \pm 0.0004$, $A_2 = 0.255 \pm 0.001$, $\tau_1 = 22.01 \pm 0.04\ \mu s$ and $\tau_2 = 1.2 \pm 0.1\ \mu s$. While τ_2 is on the order of the lifetime of the $6s6p\ ^3P_1$ state, the dominant τ_1 decay is somewhat puzzling as it is much shorter than lifetimes expected for the $6s6p\ ^3P_0$ and $^3P_2$ states. The former has a 50 s lifetime in Ne,[5] and the latter has one of about 15 s in the gas phase.[13] We therefore continue to assign the 605 nm emission peak to the $6s6p\ ^3P_1$ state but suggest that either there is some overlapping $6s6p\ ^3P_{0,2}$ emission present or that the symmetry of the corresponding site causes a degeneracy in the ^3P_J states that lengthens its lifetime.[14]

Measurements were also made of the decay of the 655 nm and 710 nm emission peaks and from the single exponential fits the values of $13.30 \pm 0.02\ \mu s$ and $387.7 \pm 0.3\ \mu s$, respectively, were obtained at 4.8 K. These lifetimes may be compared to the values of τ_1 for the 605 nm peak. Due to the weakness of the 655 nm and 710 nm features we cannot be completely confident in this data (uncertainties given solely reflect the quality of the fits) and leave more careful analysis to future work. Nonetheless, the above

TABLE III. Lifetimes of the normalized decay profiles of the 564 nm emission from an annealed sample at different temperatures. The lifetime, τ, is obtained from a fit of the curve of normalized counts against time, t, to a single exponential of the form $NC = e^{-t/\tau}$ for the 564 nm emission. For the 605 nm peak a double exponential of the form $NC = A_1 e^{-t/\tau 1} + A_2 e^{-t/\tau 2}$ is used.

T, K	564 nm τ, ns	605 nm τ_1, μs	605 nm τ_2, μs
4.8	382 ± 2	22.01 ± 0.04	1.23 ± 0.01
10	369 ± 2	25.75 ± 0.05	1.23 ± 0.01
15	353 ± 2	25.55 ± 0.05	1.16 ± 0.01
20	329 ± 2	28.06 ± 0.06	1.15 ± 0.02
25	306 ± 2	27.24 ± 0.05	1.23 ± 0.02
30	283 ± 2	27.23 ± 0.05	1.53 ± 0.04

FIG. 4. Normalized decay profiles of the 564 nm emission from an annealed sample. For reasons of space, the top panel groups together the results at 4.8, 15 and 25 K, while the bottom panel groups together those at 10, 20 and 30 K. The life-times, τ, given by a single exponential fit to the data, are presented in the legend.

hypothesis on the mixing of the $6s6p\ ^3P_J$ emissions can be considered a provisional explanation.

Further indications that the emission peaks are due to distinct trapping sites can be found in the Fig. 3, which illustrates the
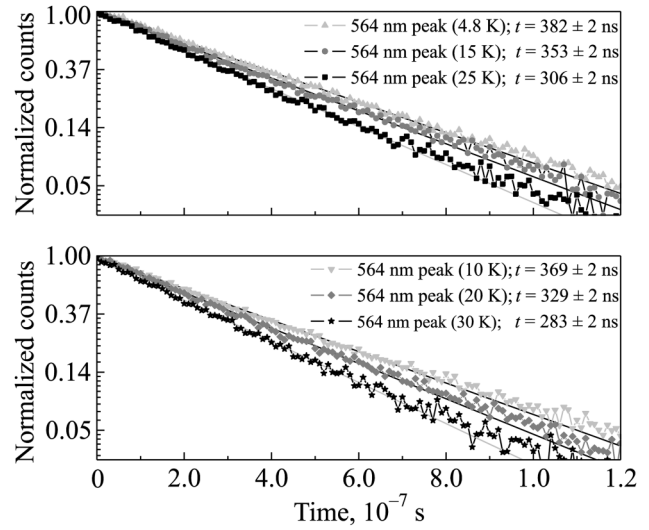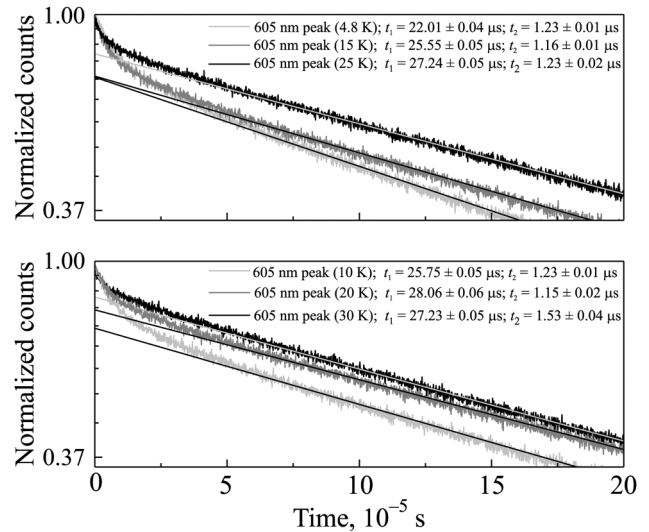

FIG. 5. Normalized decay profiles of the 605 nm emission from an annealed sample. For reasons of space, the top panel groups together the results at 4.8, 15 and 25 K, while the bottom panel groups together those at 10, 20 and 30 K. The lifetimes, τ_1 and τ_2, given by a double exponential fit to the data, are presented in the legend.

peculiar effects of annealing and irradiation on the Yb/Xe sample. In the unannealed sample, the 605 nm peak slightly dominates the emission spectra. As one continues to excite the singlet transition, the 564 nm peak grows at the expense of the 605 nm one. A more dramatic shift in the same direction is observed after annealing the sample to 30 K for 10 minutes and then cooling it back to 4.8 K. This results in the clear domination of the 564 nm peak over the 605, 655 and 710 nm peaks, with the latter two significantly reduced. Within the range of 4.8–30 K, these changes are perfectly reversible so that cooling the sample back to 4.8 K restores the amplitudes of the peaks to their original values given by the solid trace in the Fig. 3.

Stable evolution upon heating as illustrated by Fig. 6 made it possible to measure 564 nm and 605 nm emission lifetimes as a function of temperature. The τ_1 and τ_2 life-times of the 605 nm emission are essentially constant, while that of the 564 nm emission declines steadily with increasing temperature, as shown in Table III. As we discuss in Sec. 4, the latter can be described by non-radiative relaxation assisted by electron–phonon coupling, which competes with the radiative decay channel.

4. DISCUSSION

4.1. Matrix trapping sites

To interpret the structure of the absorption spectrum, we performed classical modeling of the trapping site stability, closely following the approach proposed in Refs. 9 and 15. For this purpose, the interaction potentials of the Yb–Kr and Yb–Xe complexes in the ground $^1\Sigma^+$ state were calculated *ab initio* by means of the single-reference coupled cluster method with singles, doubles and

FIG. 6. Emission spectra of the Yb/Xe system excited with a laser centered at 405 nm showing the temperature dependence of the annealed sample.

non-iterative correction to triples, CCSD(T).[16,17] The ECP28MDF effective core potentials were employed for Yb[18] and Xe[19] atoms, whereas their ECP10MDF analog[19] was employed for Kr. For the Yb atom, the supplementary basis set was used augmented by the set of diffuse spdfg primitives continuing the smallest exponents in each symmetry type as an even-tempered sequence. The Kr and Xe atoms were described with the augmented correlation consistent polarized quadruple-zeta bases aug-cc-pVQZ.[19] To further saturate the dispersion interaction, the $3s3p2d2f1g$ set of bond functions[20] was added in the middle of the internuclear distance. Reference orbitals were generated by the restricted Hartree–Fock method; the Yb and Xe core consisted of the $4s^2 4p^6 4d^{10}$ shells, while the Kr core consisted of the $3s^2 3p^6$ shells. Counterpoise correction[21] for the basis set superposition error was included.

Parameters of the *ab initio* Yb–Kr, Xe and Yb–Ar[9] interactions, namely, the location of the inflection point σ, $V(\sigma)=0$, the equilibrium distance R_e and the well depth D_e, are given in Table IV. These potentials, together with the well established potential functions by Aziz and co-workers for Ar–Ar, Kr–Kr and Xe–Xe dimers,[22–24] were used as the pairwise potential energy surfaces (PESs) that determine the site structure and stability as described elsewhere.[9,15]

The energies of the lowest structures found for the Yb atom in Ar,[9] Kr and Xe are depicted in Fig. 7 as a function of n, the number of RG atoms removed from the lattice to accommodate the Yb atom. The stable structures are those which form the convex hull, i.e., possess the energy lying below any line on the (E, n) plane connecting two other points. In all the hosts, three structures, $n = 1$, 4 and 6, satisfy this criterion. Analysis shows that the $n = 1$ structure corresponds to the single substitution site, in the $n = 4$ structure Yb is placed inside the tetravacancy formed by removal of the vertex and three nearest face-centered host atoms, while in the $n = 6$ structure Yb occupies the hexa-vacancy with all the face-centered atoms of the unit cell are removed. However, the relative stability of the three sites varies strongly from Ar to Xe. In the former case, in agreement with the experiment on the site interconversion kinetics,[9] the tv structure is the ground blue trapping site, while the secondary hv structure manifests itself as the violet site. Occupation of the third red ss site was found to be low. By contrast, in Xe the ss structure corresponds to the most stable site. The tv is higher in energy than the ss structure in Xe by approximately the same amount that the hv structure is higher than the tv structure in Ar. This means that both ss and tv sites may well be occupied simultaneously in Yb/Xe. By similar reasoning, a low population can be expected in Xe for the third hv site. Overall, the observed trend in site stability is what should be expected for the close-packed RG crystals where the volume of the vacancies increases from Ar to Xe.
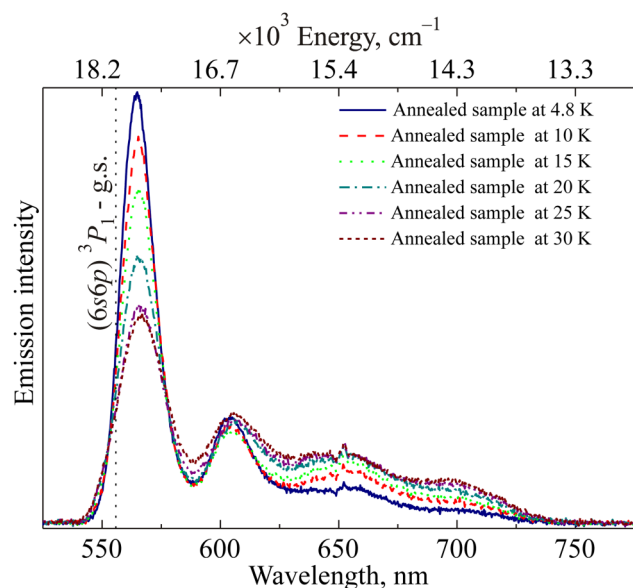
TABLE IV. Parameters of the pairwise $^1\Sigma^+$ Yb–RG potentials: the inflection point σ, the equilibrium separation R_e and the well depth D_e.

System	σ, Å	R_e, Å	D_e, cm^{-1}
Yb–Ar	4.37	5.03	69
Yb–Kr	4.30	4.98	106
Yb–Xe	4.37	5.07	150

In the case of Yb/Ar, we were able to deduce the vertical $6s^2$ $^1S_0 \rightarrow 6s6p$ $^1P_1$ transition energies for each site using the diatomics-in-molecule (DIM) approach and the Yb($^1P_1$)–Ar potentials V_Σ and V_Π of the Σ and Π symmetry.[9] These potentials are not presently available for Yb($^1P_1$)–Xe pair. However, speculating on the previous Yb/Ar results, we may suggest that the absorption frequency in isolation increases with the effective volume of the site, from ss to hv. This leads us to the tentative association of the features identified in the absorption spectra with the stable sites found by modeling: the violet peak corresponds to hv occupation, the blue peak corresponds to tv occupation and the red shoulder corresponds to ss occupation. Annealing effects corroborate this interpretation showing the depopulation of the least stable (violet, hv) site in favor of the most stable (red, ss) one. The blue feature exhibits intermediate behavior, as should be expected for tv occupation.

The effects of annealing and irradiation on the emission spectra can be explored in an attempt to link the emission and absorption features, assuming that each site produces one dominant emission band and that the population transfer between the sites occurs mostly in the ground state. The same assumptions allowed us to explain the variations of Yb emission in the Ar matrix.[9] It was found that Yb predominantly occupies the most stable tv blue site in the unannealed Ar sample though it can be transferred to the second stable violet hv sites by heating.

As shown in Fig. 3, annealing strongly diminishes the amplitude of the 605 nm Yb/Xe emission peak in favor of the 564 nm one. It is therefore reasonable to identify the red 412 nm absorption shoulder with the 564 nm emission, while the violet 402 nm absorption peak can be identified with the 605 nm emission. Thus, predominant occupation of the least stable but the most spacious violet hv sites at deposition is suggested, in contrast to the Yb/Ar case. This difference, however, also manifests itself in the observed effect of irradiation. In the Ar matrix, irradiation has the opposite effect of annealing, inducing a population transfer from the higher-lying violet hv to the ground blue tv site. In the Xe matrix, irradiation and annealing cause a population transfer in the same direction, from the higher-lying violet hv site to the ground red ss site.

After annealing further population changes can be induced by heating and cooling, though not by irradiation. While these observations further support our plausible site assignments, they also indicate that heating to only 35 K may be insufficient to completely anneal the sample, leaving a fraction of Yb atoms in the least stable occupation.

The dependence of emission on temperature shown in the Fig. 6 further supports the above assignments. Heating depopulates the most stable red site at 564 nm while having almost no effect on the violet site at 605 nm. As a result, the population is redistributed towards the weaker 655 nm and 710 nm emission peaks, at least one of which may belong to the intermediate blue site.

Although the above interpretation provides consistent explanation for the most of absorption and emission observations and is supported by trustworthy site stability modeling, we still consider it to be tentative. More direct confirmation should emerge from excitation spectral measurements and better characterization of the site transformation effects by means of annealing to higher temperatures and higher temperature deposition.

4.2. Non-radiative decay and electron–phonon coupling

The first stage of the relaxation pathway—from the singlet to the triplet state—must occur on the order of a few nanoseconds in order to quench the emission from the excited bright $6s6p$ $^1P_1$ state whose gas-phase lifetime is 5.7 ns. Our earlier works attributed this to a matrix-induced curve crossing between the PESs of the close-lying $6s5d$ ^3D_J and $6s6p$ $^1P_1$ states.[8,9] In solid Xe, additional curve crossings between the PESs of the ^3P_J states and the above-mentioned ones may also be a factor, as has been studied for the Zn/Xe system.[25] This results in a highly efficient non-radiative singlet-to-triplet intersystem crossing rate which leaves the $6s6p$ $^3P_1 \rightarrow 6s^2$ $^1S_0$ transition—the second stage in the relaxation pathway—as the principal bottleneck in the decay to the ground state. This second stage can occur by radiative and non-radiative pathways, the latter of which results in the temperature-dependence of the decay at 564 nm.

Similar observations have been made for a number of matrix isolated species whose low-lying states have temperature-dependent lifetimes, though without the nature of the non-radiative process being made explicit.[14,26] In the present case, we show that the process can be described as electron–phonon coupling, by which lattice vibrations promote an electronic transition from an excited state to one lower by a quantum of lattice mode energy, $\hbar\omega_m$, through the emission of a phonon at characteristic mode frequency ω_m. Since ω_m is on the order of the Debye frequency, multiple phonon emission is required to bridge the relatively large gap between the excited and ground electronic states. The non-radiative decay rate of the excited $^3P_1$ state, $W_{NR}(T)$, is equivalent to that multiphonon emission rate and its relationship to temperature, T, arises from its dependence on the Bose–Einstein occupation number, $n_m(T) = [e^{\beta\hbar\omega_m} - 1]^{-1}$, where $\beta = 1/kT$. The overall relaxation rate of the $^3P_1$ state is therefore

$$W(T) = W_R + W_{NR}(T), \tag{1}$$

where W_R is its radiative decay rate.

The precise relation of $W_{NR}(T)$ to $n_m(T)$ is given by the solution of the equation of motion arising from the electron-lattice Hamiltonian:

$$\mathbf{H} = -\frac{\hbar^2}{2m}\sum_i^n \frac{\partial^2}{\partial r_i^2} + V(\mathbf{r}, \mathbf{R}) - \frac{\hbar^2}{2}\sum_j \frac{\partial^2}{M_j \partial R_j^2}, \tag{2}$$

where $\mathbf{r}$ and $\mathbf{R}$ are the respective coordinate operators for all electrons and all nuclei, while $V(\mathbf{r}, \mathbf{R})$ includes all nuclear-nuclear and electronic-nuclear interactions. Foundational treatments of this problem have been given by Fischer[27] and Engleman and Jortner[28] within the limits of the Born–Oppenheimer adiabatic approximation. For the case of weak coupling at low temperature ($\beta\hbar\omega_m > 1$) they found:

$$W_{NR}(T)/W_{NR}(0) = 1 + \frac{\Delta E}{\hbar\omega_m} e^{-\beta\hbar\omega_m}, \tag{3}$$
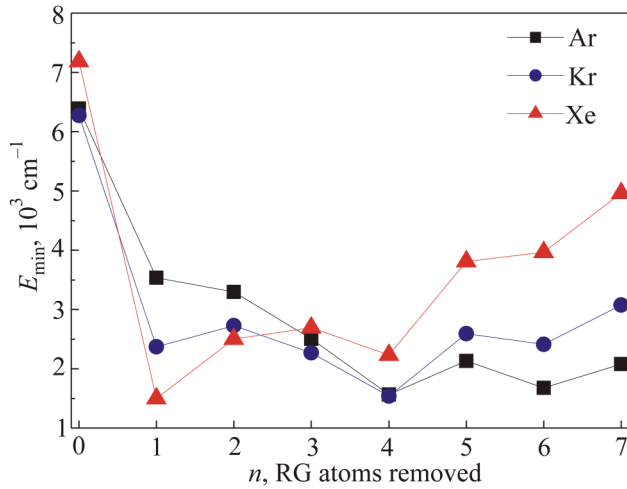
FIG. 7. Energies of the lowest structures found for the Yb atom trapped in the RG crystals with n host atoms removed. Energy origin corresponds to the ideal crystal and free atom.

where ΔE is the electronic energy gap between the two states involved in the non-radiative decay.

The above equation assumes that the relative displacement of the two adiabatic potential surfaces is negligible and that the coupling occurs to a single lattice mode of the highest frequency. For the rare-earth ions in crystals, these approximations are known to hold well for transitions involving electronic states of the $4f^n$ configuration.[29] One may expect the same for the 564 nm peak which
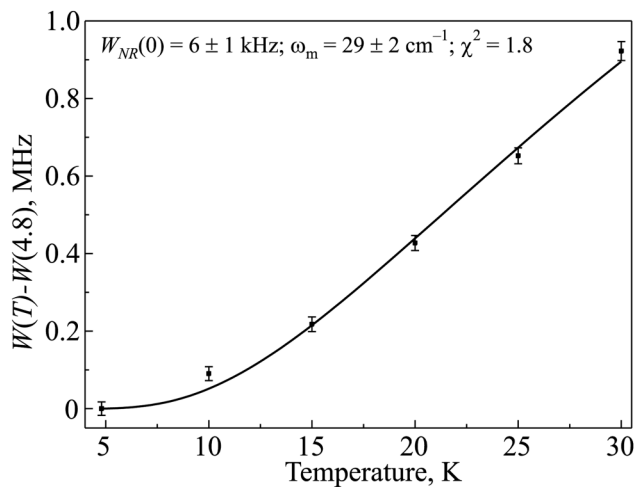

FIG. 8. Plot of the difference of the decay rates at different temperatures and the decay rate at 4.8 K [i.e., $W(T) - W(4.8)$] for the 564 nm emission. The results of a least-squares fit of the data to the expected curve in the case of electron–phonon coupling to a single mode [Eq. (4)] is also shown.

has the smallest matrix-induced frequency shift. In any case, Eq. (3) should give us an upper limit for the phonon frequency.

The total decay rate, $W(T) = 1/\tau(T)$, can be obtained from the data in Table III and the radiative decay rate, W_R, eliminated by a simple subtraction to obtain

$$W(T) - W(4.8) = W_{NR}(0) \frac{\Delta E}{\hbar\omega_m} (e^{-\beta\hbar\omega_m} - e^{-\beta(4.8)\hbar\omega_m}). \quad (4)$$

A plot of $W(T) - W(4.8)$ against the temperature is shown in Fig. 8. A least-squares fit to Eq. (4) with $\Delta E = 17733$ cm^{-1} for the 564 nm emission gave a reasonable result for the phonon frequency of $\omega_m = 29 \pm 2$ cm^{-1}. As expected, the phonon frequency is on the order of the Debye frequency for solid Xe (64 cm^{-1}), providing further support for our hypothesis. One may also note that the characteristic ground state Yb vibrational frequencies for the ss and tv sites were calculated as 30 cm^{-1} and 16 cm^{-1}, respectively. Their coupling with lattice vibrations upon energy transfer can be seen as the cause of a reduction of the effective phonon frequency.

5. CONCLUDING REMARKS

The photophysical properties of Yb in solid Xe have been studied experimentally by absorption and emission spectroscopy. For the lowest bright $6s^2 \, {}^1S_0 \rightarrow 6s6p \, {}^1P_1$ absorption, we observed a number of interesting features: quenching of the singlet emission, structured triplet $6s6p \, {}^3P_1 \rightarrow 6s^2 \, {}^1S_0$ emission with temperature-dependent decay, as well as heat- and light-induced transformations of the emission peaks.

Despite the strong congestion of the absorption spectrum, we have interpreted these findings assuming that the Yb atom occupies multiple trapping sites. We have identified three of them, labelling them "red", "blue" and "violet" according to their absorption frequencies. Simultaneous excitation of these sites results in multiple emission features, essentially different in their lifetimes and behaviours upon annealing, heating and irradiation of the sample. With the help of a theoretical site stability model and comparison with the Yb/Ar system studied previously, we have found a consistent interpretation of our main observations in the associations of the red, blue and violet sites with the ss, tv and hv occupations, respectively, in order of their decreasing theoretical stability.

Temperature-dependent lifetime measurements performed for the dominant emission features revealed their distinct kinetics. For the 605 nm peak, tentatively assigned to the least stable violet site, a double exponential decay has been observed with almost no temperature variation. In contrast, the 564 nm emission, presumably originating from the most stable red site, decays exponentially with a rate that grows dramatically with temperature. Remarkably, we have found that such dependence is accurately described by the competition of the radiative decay with vertical non-radiative relaxation assisted by electron–phonon coupling. The effective phonon frequency of 29 ± 2 cm^{-1} obtained by a least-squares fit is realistic for the Yb atom trapped in a Xe ss site.

There are still a number of aspects of this system that require further work. Decisive assignment of absorption and emission features to the different trapping site requires excitation-emission spectroscopy and a more thorough study of the effects of annealing,

while further insight into the origins of the 655 nm and 710 nm emissions can be achieved in principle by the classical modeling of the $^3P_1$ state.

ACKNOWLEDGMENTS

REFERENCES

[1]Y. Takasu, K. Maki, K. Komori, T. Takano, K. Honda, M. Kumakura, T. Yabuzaki, and Y. Takahashi, Phys. Rev. Lett. **91**, 040404 (2003).

[2]T. Fukuhara, S. Sugawa, and Y. Takahashi, Phys. Rev. A **76**, 051604 (2007).

[3]T. Fukuhara, Y. Takasu, M. Kumakura, and Y. Takahashi, Phys. Rev. Lett. **98**, 030401 (2007).

[4]N. Hinkley, J. A. Sherman, N. B. Phillips, M. Schioppo, N. D. Lemke, K. Beloy, M. Pizzocaro, C. W. Oates, and A. D. Ludlow, Science **341**, 1215 (2013).

[5]C.-Y. Xu, J. Singh, K. G. Bailey, M. R. Dietrich, J. P. Greene, W. Jiang, N. D. Lemke, Z.-T. Lu, P. Mueller, and T. P. O'Connor, Phys. Rev. Lett. **113**, 033003 (2014).

[6]See materials at https://spinlab.me/research/single-atom-microscope (Last accessed Feb 3, 2019).

[7]C.-Y. Xu, S.-M. Hu, J. Singh, K. Bailey, Z.-T. Lu, P. Mueller, T. P. O'Connor, and U. Welp, Phys. Rev. Lett. **107**, 093001 (2011).

[8]R. Lambo, A. A. Buchachenko, L. Wu, Y. Tan, J. Wang, Y. R. Sun, A.-W. Liu, and S.-M. Hu, J. Chem. Phys. **137**, 204315 (2012).

[9]L.-G. Tao, N. N. Kleshchina, R. Lambo, A. A. Buchachenko, X.-G. Zhou, D. S. Bezrukov, and S.-M. Hu, J. Chem. Phys. **143**, 174306 (2015).

[10]Y. Ralchenko, A. E. Kramida, and J. Reader, *NIST ASD Team, NIST Atomic Spectra Database (ver. 4.0.1)*, National Institute of Standards and Technology (2010), available online http://physics.nist.gov/asd.

[11]S. Suzer and L. Andrews, J. Chem. Phys. **89**, 5514 (1988).

[12]K. Beloy, J. A. Sherman, N. D. Lemke, N. Hinkley, C. W. Oates, and A. D. Ludlow, Phys. Rev. A **86**, 051404(R) (2012).

[13]S. G. Porsev, Y. G. Rakhlina, and M. G. Kozlov, Phys. Rev. A **60**, 2781 (1999).

[14]J. G. McCaffrey and G. A. Ozin, J. Chem. Phys. **89**, 1844 (1988).

[15]N. N. Kleshchina, K. A. Korchagina, D. S. Bezrukov, and A. A. Buchachenko, J. Phys. Chem. A **121**, 2429 (2017).

[16]P. J. Knowles, C. Hampel, and H.-J. Werner, J. Chem. Phys. **99**, 5219 (1993).

[17]P. J. Knowles, C. Hampel, and H.-J. Werner, J. Chem. Phys. **112**, 3106 (2000).

[18]Y. Wang and M. Dolg, Theor. Chem. Acc. **100**, 125 (1998).

[19]K. A. Peterson, D. Figgen, E. Goll, H. Stoll, and M. Dolg, J. Chem. Phys. **119**, 11113 (2003).

[20]S. M. Cybulski and R. R. Toczylowski, J. Chem. Phys. **111**, 10520 (1999).

[21]S. F. Boys and F. Bernardi, Mol. Phys. **19**, 553 (1970).

[22]R. A. Aziz, J. Chem. Phys. **99**, 4518 (1993).

[23]R. A. Aziz, Mol. Phys. **67**, 1291 (1989).

[24]A. K. Dham, W. J. Meath, A. R. Allnatt, R. A. Aziz, and M. J. Slaman, Chem. Phys. **142**, 173 (1990).

[25]W. H. Breckenridge, M. D. Morse, and J. G. McCaffrey, J. Chem. Phys. **109**, 3137 (1998).

[26]V. A. Bracken, P. N. Kerins, P. Gurtler, and J. G. McCaffrey, J. Chem. Phys. **107**, 5300 (1997).

[27]S. Fischer, J. Chem. Phys. **53**, 3195 (1970).

[28]R. Engleman and J. Jortner, Mol. Phys. **18**, 145 (1970).

[29]F. K. Fong, S. L. Naberhuis, and M. M. Miller, J. Chem. Phys. **56**, 4020 (1972).

Translated by AIP Author Services